



Correlative microstructure and topography informed nanoindentation of copper films



Stephan Bigl ^{a,*}, Thomas Schöberl ^b, Stefan Wurster ^a, Megan J. Cordill ^b, Daniel Kiener ^a

^a Department of Materials Physics, Montanuniversität Leoben, Jahnstrasse 12, 8700 Leoben, Austria

^b Erich Schmid Institute of Materials Science, Austrian Academy of Sciences, Jahnstrasse 12, 8700 Leoben, Austria

ARTICLE INFO

Article history:

Received 1 April 2016

Revised 25 July 2016

Accepted in revised form 30 July 2016

Available online 24 August 2016

Keywords:

Copper metallization

Local mechanical behaviour

Nanoindentation

Grain boundaries

Contact mechanics

ABSTRACT

The effect of residual inorganic elements on the local plastic deformation behaviour of two different copper films was investigated. It was found that a film containing inorganic elements in the ppm range, has a distinctively higher hardness at twin boundaries and high angle grain boundaries compared to the grain interior. An almost pure copper film shows no distinct difference regarding the plastic deformation compared to the same microstructural features. The results suggest that such residual elements form hard boundaries, leading to higher hardness on a local microstructural level. Moreover, the influence of the local topography was demonstrated. The use of atomic force microscopy before and after indentation illustrated that significant errors in the determination of hardness occurs when the local surface topography matches the dimensions of the indenter tip. This was further confirmed by the quantitative comparison of the elastic properties of the loading and unloading segments of the corresponding load-depth curves using Hertzian contact mechanics and the Oliver-Pharr method. It is demonstrated that the measured hardness values can be directly correlated to local microstructural and topographical features.

© 2016 Elsevier B.V. All rights reserved.

1. Introduction

In modern material science, great interest lies in the improvement of the mechanical properties of materials by modifying the initial microstructure. Especially in the microelectronics industry, the need for customized metallization layers is of great interest, satisfying the requests for high strength or microstructural stability at elevated temperatures. Copper metallizations and interconnects represent one of the key material components used in microelectronic devices. Lower cross-sectional areas, high current densities, withstanding large thermal stresses, and the on-going reduction of the volume to surface ratio are only a few challenges of copper metallization layers [1–4]. Therefore, a detailed understanding of the influence of the microstructure on the thermo-mechanical fatigue behaviour is needed to improve future copper metallizations with respect to product requirements and reliability during operational lifetime.

Strengthening mechanisms, such as the Hall-Petch effect, show that the grain size plays a key role in the enhancement of mechanical properties of bulk materials [5,6]. Such effects can also be obtained for metallic thin films. Thereby, electrodeposited copper (Cu) showed a tensile strength about ten times higher than that of conventional

(bulk) Cu while retaining bulk electrical conductivity comparable to that of pure Cu [7]. The high strength is explained by the sub-micron grain size and the dense network of coherent twin boundaries serving as an effective blockade to dislocations. At the same time, such coherent twin boundaries have an extremely low resistivity compared to other interfaces such as high angle grain boundaries (HAGB) (misorientation $\theta \geq 15^\circ$). It should be clear that mechanical properties are specifically altered via grain boundary engineering through grain refinement or the generation of a high fraction of twin boundaries. Both the grain size and presence of twins can be easily modified in copper thin films since grain size is strongly influenced by the deposition parameters and the low stacking fault energy (SFE) promotes twin formation [8]. Furthermore, impurities incorporated through the deposition process can strongly alter interfacial energies and the subsequent material behaviour such as fatigue and electromigration [9]. It becomes clear that for such microstructures, grain boundaries become the dominant component which determines the initial mechanical properties and fatigue behaviour. Hence, investigation of specific grain boundaries with respect to mechanical forces on the micro-scale is necessary to predict the overall microstructural behaviour and basic information with regards to plastic deformation.

Nanoindentation is widely used to determine mechanical properties, such as elastic modulus and hardness, of bulk and thin film materials [10]. Previous works used this method to examine changes of mechanical properties with respect to local variation of chemical composition

* Corresponding author.

E-mail addresses: stephan-paul.bigl@stud.unileoben.ac.at, [\(S. Bigl\).](mailto:stephan_bigl@hotmail.com)

and microstructure [11–14]. For such localized investigations very low penetration depths in the nm range are used, which are sometimes below the measured surface roughness, raising the question of the validity of the indentation results [15]. Even though several papers [16–27] have examined the influence of surface roughness on the determination of mechanical properties, none of those studies experimentally addressed the local contact problem in a qualitative and quantitative manner as will be demonstrated in this work.

In a recent study the thermo-mechanical fatigue behaviour of two different copper films with respect to their impurity content originating from electrodeposition were investigated [28]. The almost impurity free Cu film showed pronounced grain growth, twin boundary migration, severe surface roughening and energy minimizing texture changes. The impurity containing Cu film revealed marginal grain growth coupled with insignificant twin boundary movement, a constrained roughness evolution and almost no texture change. This indicates that even a small amount of impurity elements strongly alters the microstructural evolution with respect to HAGB or twin boundaries. Therefore, the quantification of the mechanical response of specific grain boundaries with respect to impurity levels is needed. In this work, results are presented on the comparison of the global and local deformation behaviour of two different film systems as well as specific grain boundaries with respect to the impurity content using nanoindentation. Furthermore, the challenge regarding determination of mechanical properties on a microstructural level is shown by the effect of the local contact situation (surface roughness and grain boundary grooves). Using indent-specific AFM imaging before and after indentation enables the verification of the influence of the local topography. These observations are combined with the corresponding load-displacement curves and the grain boundary character determined from EBSD images to finally evaluate the role of impurities in copper films.

2. Experimental

For all experimental investigations two different 5 µm thick copper films were used. Both film system were prepared by electrochemical deposition and sputtering, which is the current state of the art process for wafer metallization [29]. Prior to electrodeposition, a thin tungsten-based adhesion layer was sputtered on a 725 µm thick silicon wafer of (100) orientation, followed by sputtering of a 300 nm Cu film seed layer. After seed layer deposition, electrochemical deposition was utilized to create the final 5 µm thick film. This allows an artefact-free investigation of hardness and elastic modulus for low penetration depths (maximum depth: 3% of film thickness), as experimentally shown by Saha and Nix [30]. To experimentally simulate the common problem of incorporated inorganic species (e.g. Sulphur (S), Carbon (C) and Chlorine (Cl)) the deposition process was designed to result in different impurity levels by the variation of the additive contents. Film A resulted in a high remaining inorganic impurity content (≤ 100 at.% ppm), while Film B is an almost impurity-free pure copper film [31]. After electrochemical film deposition, both films were subjected to a 30 min heat treatment at 400 °C in inert atmosphere (forming gas) to guarantee a room temperature stable polycrystalline microstructure. Furthermore, the annealing step reduces microstructural defects generated during the film growth which imparts a microstructure with a low dislocation density, suitable for studying pop-in events at low strain rates [32].

Nanoindentation experiments were performed using a Hysitron Triboscope (Hysitron, Minneapolis, USA) in load control mode, an add-on instrument mounted on the scanner unit of a Dimension D3100 (Bruker Inc., Billerica, USA) atomic force microscope (AFM), which was used for AFM image acquisition. Data acquisition and analysis were done using the Triboscope 4.1.0 software package. All indents were performed using a blunt Berkovich tip ($R \sim 900$ nm) where hardness and reduced modulus were calculated using the method of Oliver and Pharr [33]. The area function (dependence of the indenter contact area on the contact depth) was determined prior to indentation using

fused silica as the calibration material ($E = 72$ GPa). For the nanoindentation experiments linear loading was applied to the prescribed maximum load, held for 15 s, and unloaded within 2 s, minimizing the influence of thermal drift on specimens sized 8 × 8 mm cut from the wafers. For global indentation experiments 25 indents were made using a loading rate of 1000 µN/s and a maximum load of 12 mN. The local microstructural investigations were carried out using 16 indents with a loading rate of 250 µN/s and a maximum load of 1 mN. Prior to performing the nanoindentation experiments, the specimens were cleaned with acetic acid at 35 °C for about 2 min to selectively etch the potentially formed copper oxide [34], and were mounted on a magnetic iron platelet using a resin. In order to use the correct machine compliance with respect to the mechanical testing, five bare silicon substrates (8 × 8 mm) were mounted the same way as mentioned above. Thereby, machine compliance was varied until determination of the elastic unloading curve resulted in the reduced modulus of silicon. The determined machine compliance, which was used for the entire experimental data sets, was 1.5 nm/mN.

Roughness determination and surface topography imaging was performed with the above mentioned AFM using tapping mode. For the roughness determination 512×512 pixels scans of $50 \times 50 \mu\text{m}^2$ were acquired, while imaging of the indents (before and after) was made with areas of $30 \times 30 \mu\text{m}^2$. Post processing was performed using the Gwyddion 2.36 software [35]. In order to identify the microstructural boundaries and orientations of each indent, electron backscatter diffraction (EBSD) was performed with a step size of 30 nm. The EBSD system consists of an EDAX Digiview Camera attached to a LEO 1525 (Zeiss Inc., Oberkochen, Germany) scanning electron microscope. The TSL Analysis software was used for EBSD image processing. For the presented inverse pole figure (IPF) images, overlaid with the image quality (IQ), a confidence index clean-up with a threshold value of 0.07 was performed.

3. Results

The distinct differences observed in the crystallographic and surface scans of the same area between Film A and B are highlighted in Fig. 1. For improved illustration HAGB (white lines), primary twin boundaries ($\sum 3$, black lines), and secondary twin boundaries ($\sum 9$, grey lines) are highlighted in the IPF-IQ images. The IPF standard colour triangle, used for every EBSD image, is displayed in Fig. 3d. It can be seen that both films exhibit a similar microstructure with no texture differences, except for the fact that Film A (Fig. 1a) has a slightly higher fraction of twins than Film B (Fig. 1c). This is supported by evaluation of a larger scan area ($150 \times 150 \mu\text{m}$) where Film A has a grain size of $2.8 \pm 0.9 \mu\text{m}$ and Film B $3.2 \pm 1.1 \mu\text{m}$, including $\sum 3$ boundaries.

The determined elastic moduli using EBSD scan data (Film A: 110 ± 31 GPa; Film B: 112 ± 30 GPa) indicate that in both samples a very similar, texture-less polycrystalline copper material was deposited. As a comparison an artificial copper-EBSD file simulating a random texture resulted in an average elastic modulus of about 109 GPa. In the EBSD and AFM images in Fig. 1, the three most common boundary types are highlighted. Boundary 1 displays a random HAGB. In both samples, this particular interface results in a defined grooved boundary between neighbouring grains, displayed by the AFM images (Fig. 1b, d). Boundary 2, highlighting a primary twin ($\sum 3$) generates a defined groove-like substructure similar to the HAGB in Film A. For Film B (Fig. 1c, d) a similar correlation was not observed. Rather, primary twins (black lines) do not show any distinct morphological feature in the AFM image. Boundary 3 illustrates a secondary twin ($\sum 9$) which exhibits grooving in both films. Further investigation will not include the particular deformation behaviour of secondary twins due to the fact that secondary twins are a seldom feature in both films (Fig. 1a, c). Regarding the surface roughness, Film A has a root mean square (RMS) surface roughness of ~ 17 nm and Film B reaches a value of ~ 60 nm. Film A has a very smooth inner grain surface where height differences only appear in the form of grooves at HAGB and twin

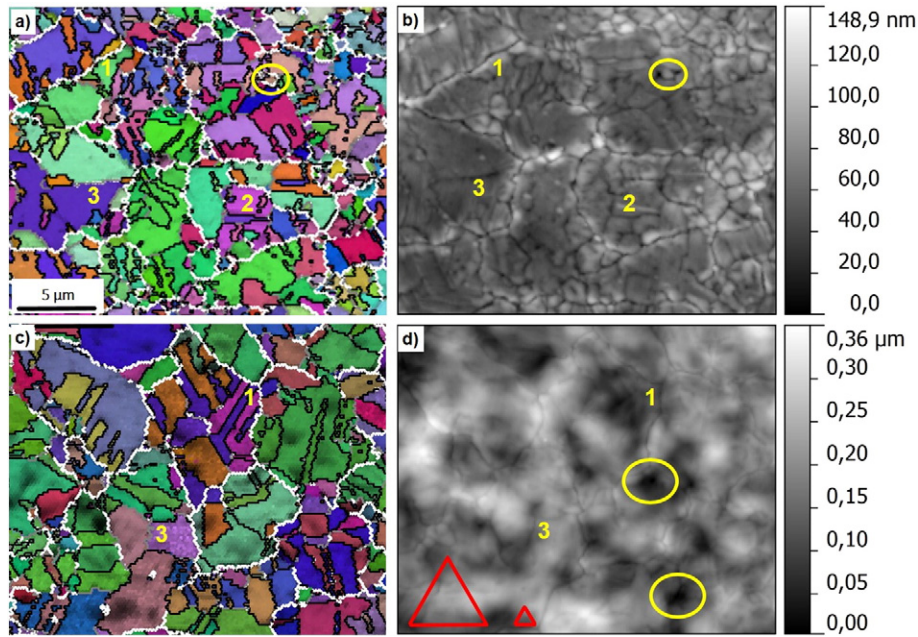


Fig. 1. Initial microstructure of Film A (a) and Film B (c) illustrated by IPF-IQ images, matching the same area of surface topography for Film A (b) and Film B (d). Interfaces such as HAGB (1), primary twins (2) and secondary twins (3) are highlighted. Furthermore, topographical features are highlighted using circles and the approximate residual indent contact areas are shown for Film B (d). Scale bar in (a) is valid for all images.

boundaries (circular feature, Fig. 1b). On the contrary, Film B has a very wavy and rough surface with strong local variation of surface curvatures and craters (indicated by circles). These distinct differences in the surface morphologies become even more important when looking at the two triangular shapes in Fig. 1d which illustrate the approximate remaining indent contact areas of the performed indentation experiments. One can anticipate that the local topography can cause

problems in the determination of site specific properties, e.g. when indenting into the craters.

Furthermore, it should be indicated that for indentation experiments performed with a high load of 12 mN (Fig. 2a), the plastically influenced area is significantly larger compared to the indentation experiments performed with a maximum load of 1 mN. This means that indentation measurements performed with the high load will measure the global

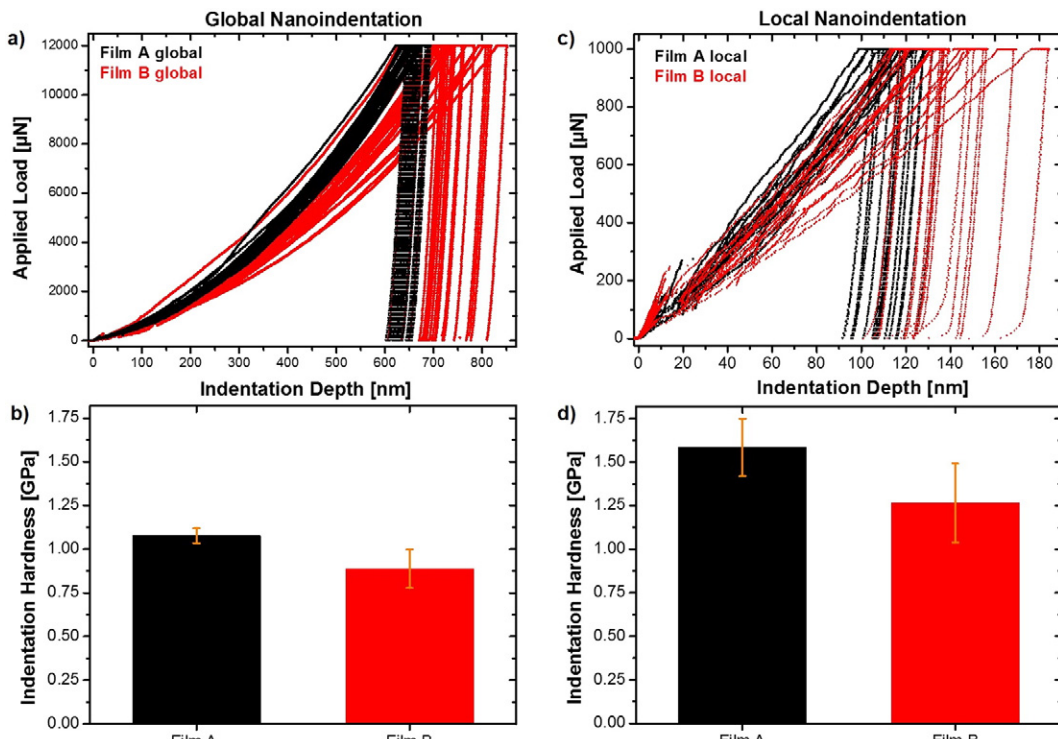


Fig. 2. Global hardness results of Film A and Film B (b) with corresponding load-displacement curves (a) are shown on the left-hand side. On the right-hand side local hardness results of Film A and Film B (d) and corresponding load-displacement curves (c) are illustrated.

deformation behaviour because it involves a representative microstructural area and the low load indents sample the local grain boundary behaviour. Fig. 2b shows the hardness for the global indentation experiments. The 25 indents for each sample resulted in an average hardness of 1.08 ± 0.04 GPa for Film A and 0.89 ± 0.11 GPa for Film B. Compared to Film B, Film A has a 21% higher hardness, a distinct difference in the mechanical properties.

In addition, it can be seen that for the experimental variance Film A has an almost three times smaller standard deviation (indicated by error bars) than Film B. The experimental variance becomes evident when the corresponding load-displacement curves are compared. All load-displacement curves (Fig. 2a) lie within a small range for the smooth Film A, but Film B has a greater scatter. Besides the scattering, the load-displacement curves confirm a systematic difference in hardness because the two data sets are distinctively separated with respect to the final indentation depth. To understand the difference in the plastic deformation behaviour and to cancel out any effect of grain size (effect of Taylor hardening as a dependence of grain size), indentation experiments were performed at the local microstructural level. Fig. 2d displays the hardness for the 1 mN indentation experiments using a maximum load of 1 mN. Film A resulted in an average hardness of 1.58 ± 0.16 GPa and 1.26 ± 0.23 GPa for Film B. Similar to the high load indentation results, Film A reveals a 25% higher hardness compared to Film B. The reason that local hardness results are significantly higher than the global hardness is due to the well-known indentation size effect [36,37]. At the same time the standard deviation of the hardness of Film A increased by a factor of four which can be attributed to the localized situation of each particular indent. In the case of Film B only an increase of a factor of two for the standard deviation was observed. When looking at the corresponding load-displacement curves (Fig. 2c) one can see that on the local scale there is an overall difference between the indents in Film A and B, although the general trend remains the

same. Two exemplary indents are shown in Fig. 3 with high resolution EBSD scans taken of each indent illustrating the crystallographic situation of Film A (Fig. 3a) and Film B (Fig. 3b) after indenting at a HAGB. The hardness for the indent in Film A was 1.37 GPa, the indent in Film B resulted in a hardness value of 0.94 GPa. This presumes that in Film A the plastic deformation behaviour distinctively deviates from that found in Film B. The load-displacement curves (Fig. 3c) confirm this with the initial elastic loading followed by a rapid excursion in depth at constant load (pop-in), indicating the onset of plastic deformation. Since further loading follows a geometrically necessary load-displacement curve, which is dependent on the particular flow stress of the material [32], the example in Fig. 3 indicates that Film A and B reveal different local plastic deformation behaviour. After the pop-in event, Film B shows a significantly flatter loading curve than Film A, resulting in the lower hardness value.

To make any appropriate conclusions regarding the differences in the local deformation behaviour further information is needed since it is not clear where the strengthening in Film A compared to Film B originates. EBSD images alone cannot provide detailed information about the exact position of the indent (see Fig. 3a,b). Experimental errors due to the local surface topography (grain boundary grooves and roughness) cannot be evaluated with the crystallographic information. Therefore, another set of indents (16 indents of each film material) was performed to determine the local deformation behaviour with respect to boundaries and topography, where additional AFM images were acquired before and after the indentation experiments. Such topography imaging before and after indentation also allows for the explanation of the large scatter observed in the load-displacement curves of Film B illustrated in Fig. 2.

Insights into such experimental errors and the demand for the critical analysis of the load-displacement curves using AFM-supported topography information are shown in Fig. 4. Two distinct experimental

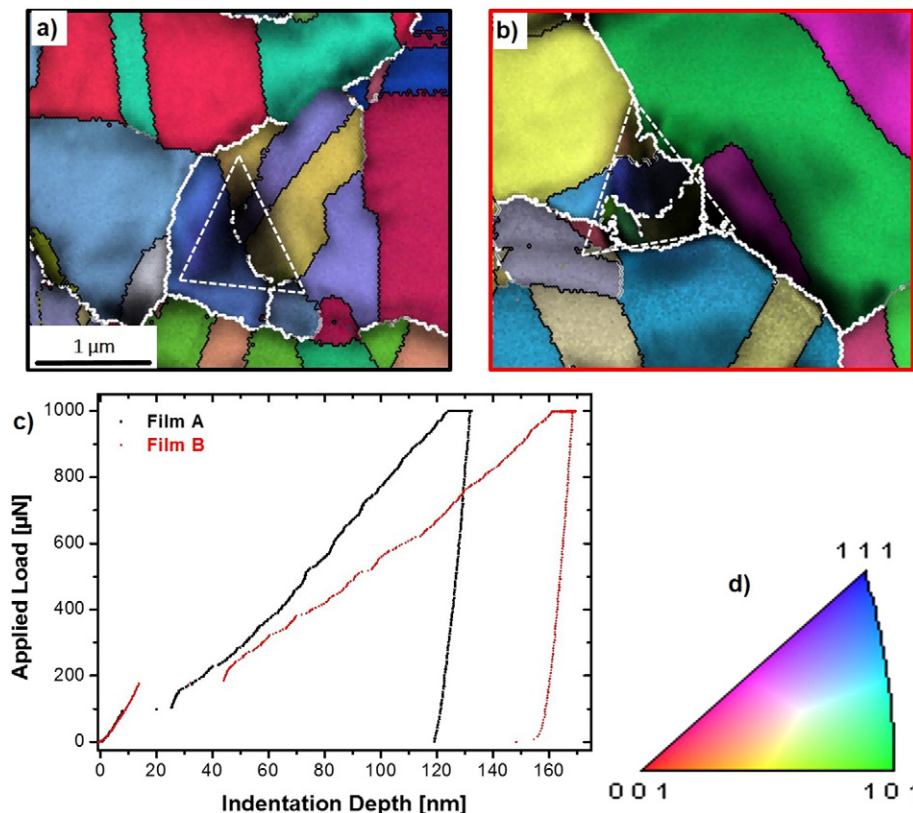


Fig. 3. High resolution EBSD images (IPF-IQ) of Film A (a) and Film B (b) after local indentation at HAGB. The corresponding load-displacement curves illustrate the difference in plastic deformation. IPF colour code (d) is applicable for all EBSD images.

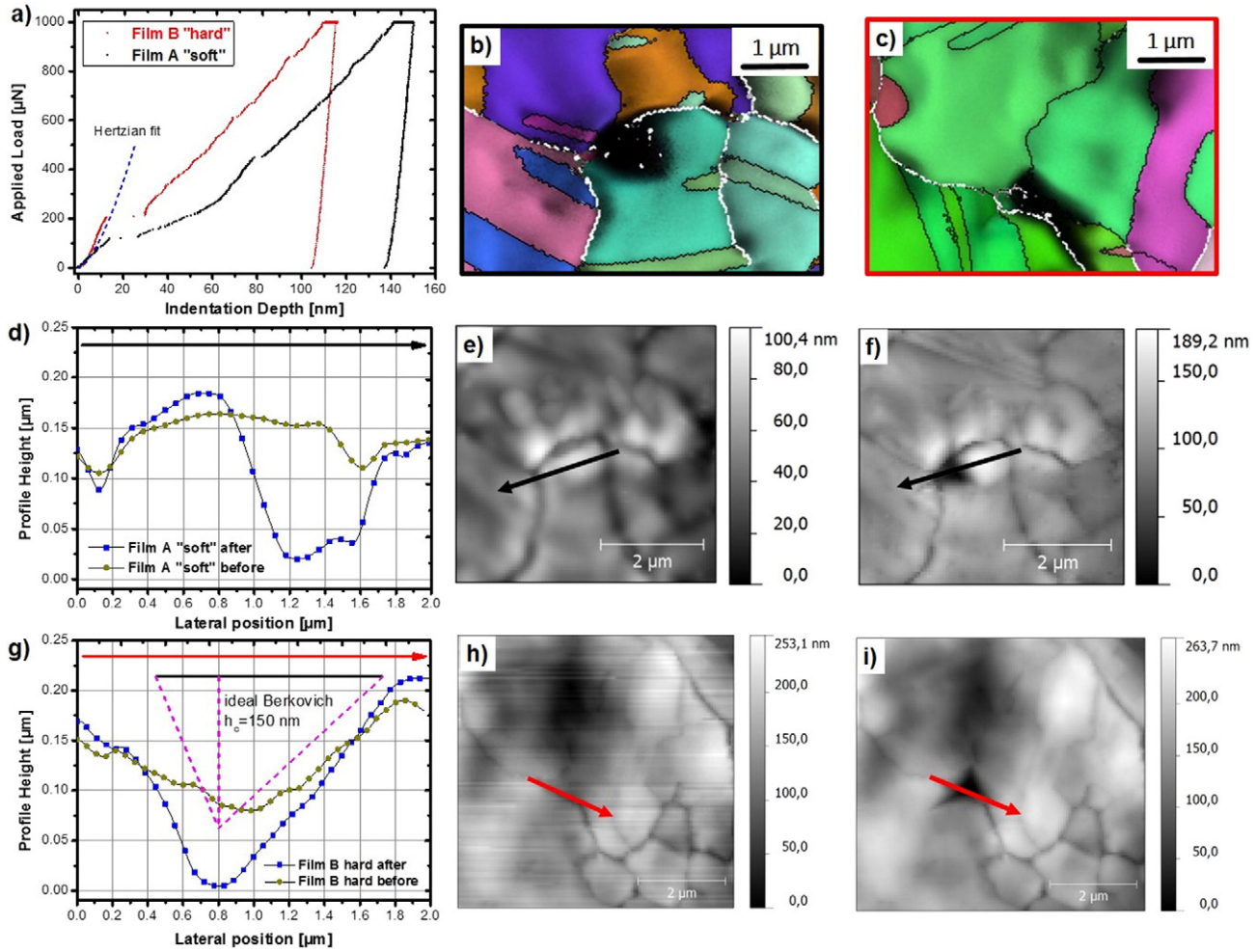


Fig. 4. Load-displacement curves (a) of situations where localized contact problems between indenter tip and surface led to erroneously determined contact areas. The initial elastic loading of the indents is described with Hertzian contact mechanics (Hertzian Fit: $E^* = 110 \text{ GPa}$, $R = 900 \text{ nm}$). Indentation at the edge of a grain in Film A (b, d-f) leads to sideward slipping of the indenter tip (a) and a lower hardness. In Film B (c, g-i) the local topographical situation, indicated with respect to the shape of a perfect Berkovich indenter geometry, led to a very steep loading curve (g) and therefore a higher hardness value.

errors are shown. Both can be attributed to a contact problem leading to an incorrect hardness value. In the case of the harder Film A, an experimental situation is shown in Fig. 4b, d-f where the indentation

at an edge of a HAGB led to a hardness value of 1.13 GPa, which distinctively differs from the mean value and its experimental variation ($1.58 \pm 0.16 \text{ GPa}$).

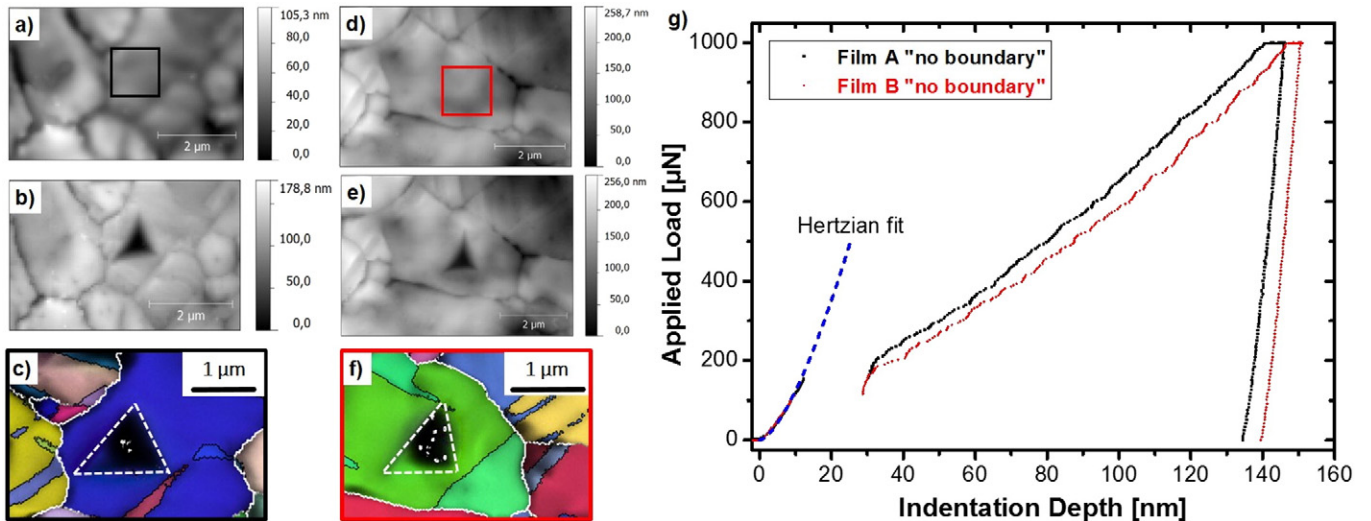


Fig. 5. Local indentation experiments in a coherent regions. AFM images before and after indentation are shown in combination with the particular crystallographic situation for Film A (a-c) and Film B (d-f). The corresponding load-displacement curves (g) show that within a grain the plastic deformation behaviour does not differ much and similar initial elastic loading following Hertzian theory is observed (Hertzian Fit: $E^* = 110 \text{ GPa}$, $R = 900 \text{ nm}$).

By taking a closer look at the load-displacement curve (Fig. 4a), it can be seen that during the loading segment flatter elastic loading compared to Film B was recorded, followed by a pop-in and a very flat increase of the load up to about 70 nm (initial loading in Figs. 4–7 is indicated by using Eq. (1), where $E^* = 110$ GPa and $R = 900$ nm, see below). When looking at the two profile sections before and after indentation (Fig. 4d) taken through the cross-section of the indenter tip from the two AFM images (arrows in Fig. 4e, f), one can see that the indenter tip has contact with the corner of a grain. The residual cross-section suggests that during the initial loading (up to ~70 nm) the tip did not have full contact with the surface. The tip appears to be sliding along the surface. With further loading, the tip follows a typical elasto-plastic loading curve (parallel to second curve). The sliding phenomenon becomes even more plausible when looking at Fig. 4g where the profile section before indentation follows approximately the shape of an ideal Berkovich indenter (drawn to scale), which is not the case for the indent in Film A (Fig. 4d).

The second experimental error illustrates the influence of the local topography, shown for an indent on the surface of Film B (Fig. 4c, g–i). It can be seen that the indenter tip was placed in an area where the local asperities match the indenter geometry to a certain extent (laterally, as well as the contact angle). The profile of an ideal Berkovich tip ($h_c = 150$ nm) indicates that during loading the contact area is significantly increased, resulting in a greater stiffness response and a steeper load-displacement curve (Fig. 4a). This led to an apparent hardness of 1.65 GPa, significantly higher than the mean value (1.26 ± 0.23 GPa), showing that local topography can lead to a severe overestimation in hardness.

After elimination of such contact problems, three representative situations with respect to grain boundaries are presented in Figs. 5–7 and the experimental analysis is supported by AFM imaging. Fig. 5 illustrates the case of the deformation behaviour in the grain interior (no boundary involved) of the two films. AFM images before and after indentation are shown in combination with the particular crystallographic situation for Film A (Fig. 5a–c) and Film B (5d–f). The EBSD and AFM images indicate that in both films no grain boundaries are present during the indentation experiments. The fact that the out of plane crystal orientation is not the same (Film A ~{111}, Film B ~{110}) can be neglected for the plastic deformation behaviour in copper since the plastic strain field under the indenter tip leads to activation of multiple slip systems and an averaged hardness of these slip systems [38]. The AFM images

show the identical surface areas which allow the evaluation of the indentation sites. The specific areas (marked as rectangles) prior to nano-indentation were investigated using profile sections for Film A (Fig. 5a) and Film B (Fig. 5d). Indentation experiments would have been discarded if potential errors, such as topography-induced indentation artefacts (addressed in the discussion) occurred. In the presented results the pre-indent surfaces do not show any tilted surfaces or cavities which could influence the indentation experiments. This can be also seen in the load-displacement curves (Fig. 5g) of the two indents. Both indents show an initially elastic loading behaviour, followed by spontaneous pop-ins at similar load/pop-in length and further similar deformation behaviour. This led to a hardness of 1.17 GPa for Film A and 1.12 GPa for Film B, indicating that within the grain interior no differences in the mechanical response is detected.

The local deformation behaviour for Film A and B begins to distinctively deviate when it comes to interactions with grain boundaries. Fig. 6 shows indentation experiments which were performed directly at a $\Sigma 3$ twin boundary. As one can see, Film A (Fig. 6a–c) shows a different deformation behaviour to Film B (Fig. 6d–f). The two films deviate in their load-displacement curves (Fig. 6g) after reaching the yield stress (pop-in). Therefore, a hardness value of 1.41 GPa for Film A and 1.02 GPa for Film B was obtained, suggesting that in Film A notable resistance to plastic deformation near the twin boundary is observed, which is not the case for Film B.

An even greater difference was observed when it comes to the interaction with HAGB. Fig. 7 illustrates the situation where indents in both films were performed at the grooved HAGB. For Film A (Fig. 7a–c) the pop-in occurs at a load of ~344 μ N with a corresponding length of 17 nm (see Fig. 7g). In comparison, Film B shows an overlapping elastic loading up to 144 μ N and pop-in length of 22 nm. This qualitatively indicates that Film A withstands higher elastic shear stresses when it comes to grain boundaries and also shows a higher flow stress than Film B. Therefore, the two load-displacement curves resulted in a hardness of 1.57 GPa for Film A and 1.02 GPa for Film B.

4. Discussion

With respect to the results shown in the previous section, two main topics will be discussed in more detail. First, the possible experimental errors (roughness, indenter shape) which become important when local indentation experiments are performed. Secondly, the material

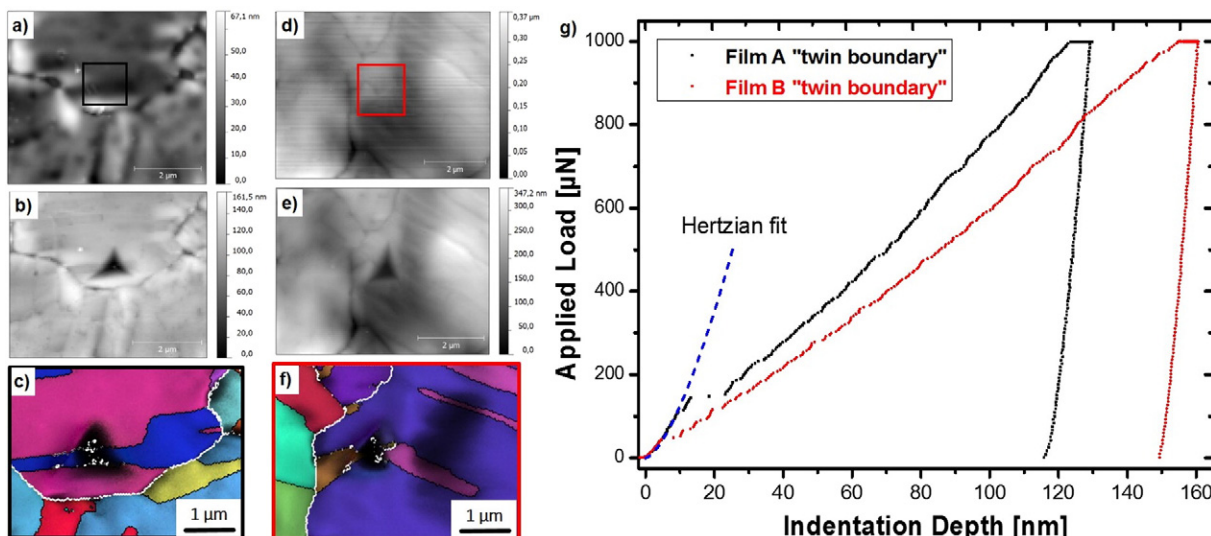


Fig. 6. Local indentation experiments at twin boundary interfaces. AFM images before and after indentation are displayed in combination with the particular crystallographic situation for Film A (a–c) and Film B (d–f). The corresponding load-displacement curves (g) show a distinct difference in the plastic deformation behaviour between the two film systems, but similar initial Hertzian elastic loading (Hertzian Fit: $E^* = 110$ GPa, $R = 900$ nm).

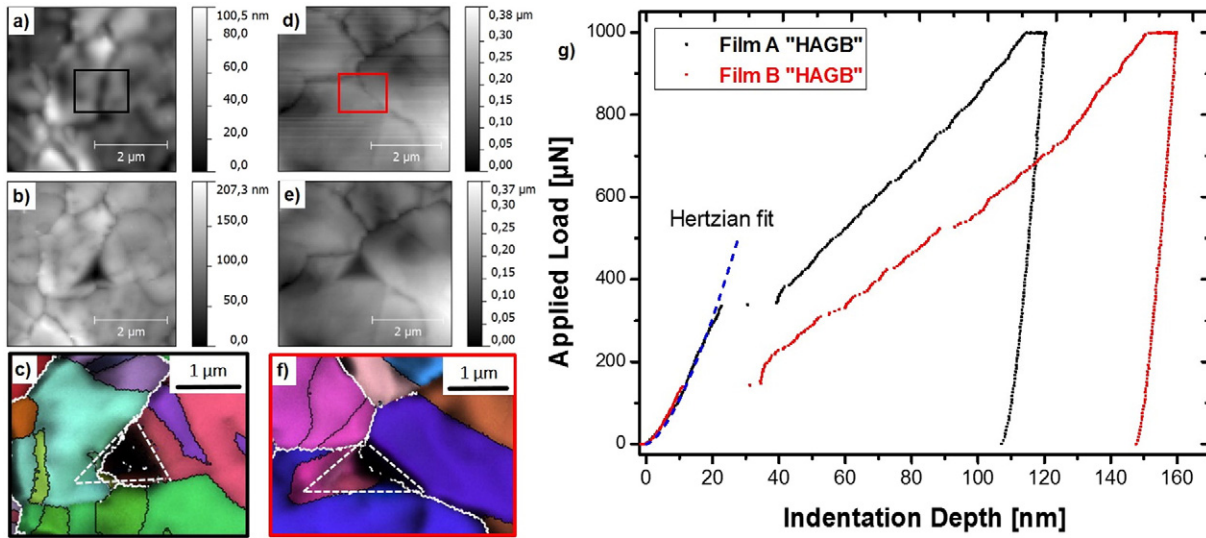


Fig. 7. Local indentation experiment at a HAGB interface. AFM images before and after indentation are illustrated in combination with the particular crystallographic situation for Film A (a–c) and Film B (d–f). The corresponding load-displacement curves (g) show that indentation for Film A resulted in a high pop-in load and lower contact depth compared to Film B, along with similar initial Hertzian elastic loading (Hertzian Fit: $E^* = 110$ GPa, $R = 900$ nm).

inherent differences in the local deformation behaviour of the two film systems with respect to boundaries and the concentration of residual inorganic elements.

4.1. Dependence of material properties on topography-induced errors

In order to substantiate the overall result that Film A has a higher hardness due to distinctively different deformation behaviour at grain boundaries, possible experimental errors will be discussed. When looking at Fig. 2 the experimental scatter of the load-displacement curves becomes evident. On a global as well as local scale, the hardness is higher for Film A than for Film B, with a higher deviation from the mean. Indentation on a global scale (12 mN load) can be seen as hardness test involving a representative volume of each sample including twins, HAGB and grain interiors, while the localized indents (1 mN) lead to area-specific indents that are influenced by the local surface topography. Such topographical contact errors were illustrated in Fig. 4, where AFM imaging revealed that local contact difficulties can lead to a significant error in the obtained load-displacement curve, thus, giving incorrect hardness values. To quantify the local influence of the topography, the elastic properties were evaluated from the examples in Fig. 4. The elastic loading in both films (Fig. 4a) prior to pop-ins should be well-described by Hertzian contact theory [39]. In the examples presented in Figs. 5–7, elastic loading segments were almost perfectly overlapping, indicating a similar elastic response and reliable indentation data. This is not the case for the presented load-displacement curves in Fig. 4 and a comparison of the reduced elastic moduli, E^* , from the loading and unloading curves support the experimental contact error. Therefore, elastic loading and unloading segments of the curves in Fig. 4a are compared to the load-displacement curves of Fig. 5g, which will be used as a reference since the indents were in a grain interior. The reduced elastic modulus, E^* , was determined from the initial elastic loading segment with Hertzian theory (Eq. (1)) and from the unloading curves using the Oliver-Pharr method [10,33]. In order to evaluate E^* , Hertzian contact mechanics is used for the first tens of nanometres where the required load P is related to:

$$P = \frac{4}{3}E^*\sqrt{Rh^3} \quad (1)$$

with R as the radius of the indenter tip (900 nm) and h the depth of penetration [40].

In Table 1, the E^* determined from the initial loading and unloading curves for Figs. 4a and 5g are compared for both films. By comparing these values the determined elastic moduli from the EBSD scans of the two films mentioned in the Results section (Film A: 110 GPa, Film B: 112 GPa) and neglecting the slight changes due to the elastic influence of the indenter and the substrate material at such indentation depths [30], one can conclude the following: For the indents with the experimental errors presented in Fig. 4, the E^* calculated with Hertzian theory and the Oliver-Pharr method do not correspond to one another as they should for either film system. The difference in elastic modulus implies different elastic material behaviour during loading and unreliable indentation data. Considering that both films represent a texture-less polycrystalline copper material this directly indicates an error in the indenter contact, which translates to a miscalculation of the contact area, A_c , necessary for accurate elastic modulus and hardness measurements using the Oliver-Pharr method. In case of the topography-evaluated indents from Fig. 5, the determined reduced elastic moduli (both loading and unloading segments) are close to the elastic modulus determined with the EBSD data (Film A: 110 GPa, Film B: 112 GPa), indicating that indents were not affected by experimental contact errors.

To further substantiate such local contact problems, Fig. 8a illustrates the influence of the topography with respect to the indenter geometry. In Fig. 8a, a 30 μm line profile for each film is presented. The direct comparison indicates that Film B has a rougher surface topography than Film A. In Fig. 8b a “rough” appearing surface section (highlighted by boxes) is shown in greater detail for both films. For

Table 1

Comparison of the reduced elastic moduli of Film A and Film B determined by Hertzian contact (initial loading) and the Oliver-Pharr method (unloading segment) using the corresponding load-displacement curves from Figs. 4a and 5g. Significant difference is found for the two experimental errors in Fig. 4a, whereas the topography evaluated indents from Fig. 5g exhibit very similar values.

Evaluated segment	E^* [GPa] Film A	E^* [GPa] Film B
Hertz Fig. 4a	80	155
Oliver Pharr Fig. 4a	102	139
Hertz Fig. 5g	116	128
Oliver Pharr Fig. 5g	117	108

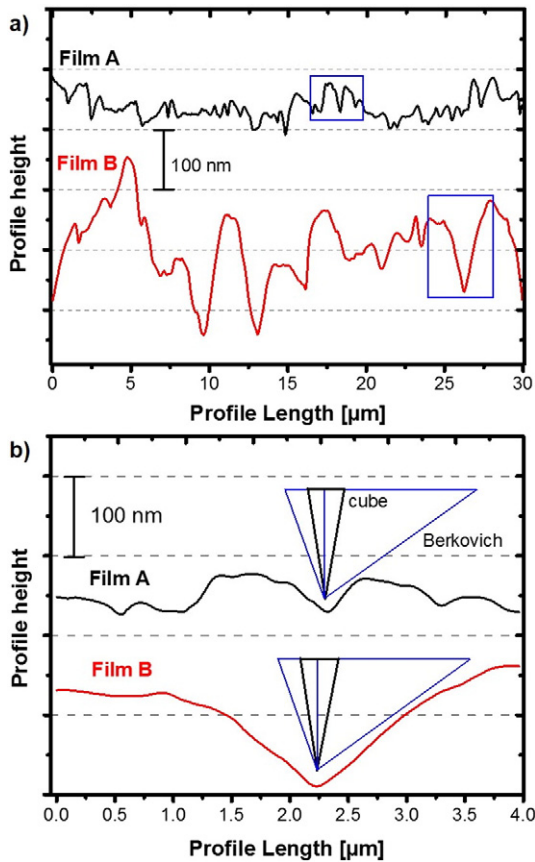


Fig. 8. Surface profiles of Film A and Film B qualitatively indicate the difference in roughness (a). Two rough surface sections are presented in more detail with respect to the topographical influence by displaying a drawn to scale Berkovich and cube corner indenter (b).

both topography situations a drawn to scale ideal cross-section (h_c : 150 nm) of a Berkovich (blue lines) and cube corner (black lines) indenter are illustrated. For the examples presented, the comparison indicates that the cube corner tip is less influenced by the local topography since its dimensions relative to the Berkovich tip are significantly smaller. This observation emphasizes that the indenter geometry can play a crucial role for certain film topographies. The surface section of Film B indicates a similar situation as already presented in Fig. 4, where the depression matches the shape of the Berkovich indenter. The particular problem does not represent the usual contact situation of a sphere [40] or a cone [41] and a half space. Therefore, an increased geometric stiffness can be expected, which would further result in a steep elasto-plastic loading curve and in unreliable hardness and E^* values.

4.2. Influence of boundaries with respect to inorganic residual elements

The reason why Film A has an overall higher hardness than Film B most likely originates from the different plastic deformation behaviour at HAGB and twin boundaries. In a previous study, chemical investigations revealed that as a result of the designed deposition processes, residual concentrations of S and Cl in the ppm range are present in Film A, which is in contrast to the almost impurity-free Cu in Film B [31]. Local chemical analysis, using laterally resolved secondary ion mass spectroscopy showed that after the annealing step, both Cl and S species accumulated at grain boundaries. This is in agreement with the current literature where such elements reveal a very low equilibrium solubility in copper-based materials [42]. The authors suggested that the segregation of such non-metallic atoms to grain boundaries

leads to embrittlement and a deterioration of the mechanical properties [31].

Figs. 5–7 illustrate the difference in the plastic deformation behaviour with respect to the influences of grain boundaries of the two films. Within the grain interior (Fig. 5), both films show a very similar deformation behaviour. This emphasizes that Film A has the same mechanical properties as Film B within coherent regions. This is also in agreement with the lateral secondary ion mass spectroscopy profiles, where most of the inorganic atom species were found at grain boundaries and do not influence the grain interior. Of note is that Film A shows a distinct grooving at twin boundaries (Fig. 1b), while grooving was not observed for Film B. The grooving is a very peculiar phenomenon, since twin boundaries are simply stacking faults composed of either Shockley or Frank partial dislocations [43]. From a thermodynamic point of view, such unusual grooving can be directly related to segregation of inorganic impurity atoms to the boundary. The morphology (depth, contact angle, etc.) of the grooves provide qualitative information on how much the free energy, G , is lowered by the minimization of the grain boundary energy, γ_g along with the rise of the surface energy, γ_s [44]. A strong decrease of interfacial energy is often related to the presence of impurities, because such interstitial atoms can bond to the matrix element and lower the energy at the free surface [45,46]. For Film B the residual concentrations of Cl and S are significantly lower and grooving is not observed. Therefore, Fig. 6 indicates that Film A has about a 40% higher hardness than Film B due to the incorporation of inorganic atomic species at twin boundaries. An even more significant difference can be seen when a HAGB is involved (Fig. 7). Besides the ~55% higher hardness of Film A compared to Film B, the corresponding load-displacement curves (Fig. 7g) indicate that for Film A a significantly higher load is needed (~335 μN) to initiate plastic deformation than for Film B (~135 μN).

These results clearly illustrate that there is a fundamental difference in the deformation behaviour when it comes to decorated twin boundaries and HAGB. In Film A the segregated inorganic elements (Cl and S) form bonds with the copper atoms at the boundaries. Both Cl and S have a high tendency to form strong ionic bonds with copper in various modifications [47]. For S the high diffusion coefficient in Cu, the high formation energy of Cu_2S (−0.14 eV/atom) and the partly covalent nature of bonding suggest the presence of very strong grain boundaries in Film A [42].

Fig. 9 schematically demonstrates the observed findings and provides a better visualisation of difference in the local mechanical properties in Film A and B. Under the complex strain field of an indenter tip many dislocations are generated due to the particular resolved shear stresses on the slip planes. In the grain interior (1) where no inorganic species are present, no obstacles result in a higher shear stress for dislocation generation and therefore, a similar (lower) hardness was observed for Film A and B. With respect to the local mechanical properties at HAGB in a pure copper material (2) the generated dislocations are absorbed at the grain boundary, but new dislocations can be easily nucleated in the neighbouring grain. Such behaviour was observed for Film B, where the mechanical properties with respect to boundaries did not deviate much compared to the hardness value obtained from the grain interior. In the case of Film A, a distinct difference of the plastic deformation behaviour was observed when a twin boundary (3) or a HAGB (4) was involved. In both cases the presence of a strong Cu-S/Cu-Cl ionic interface led to a higher resistance with respect to plastic deformation. This can be attributed to the shielding effect of such formed obstacles at the boundaries. The generated dislocations are partly blocked and a comparably higher shear stress (equivalent to a higher indenter load) is needed to further promote dislocation motion and plasticity across boundaries.

5. Conclusions and summary

It has been demonstrated that the local mechanical behaviour at grain boundaries is strongly affected by the presence of residual

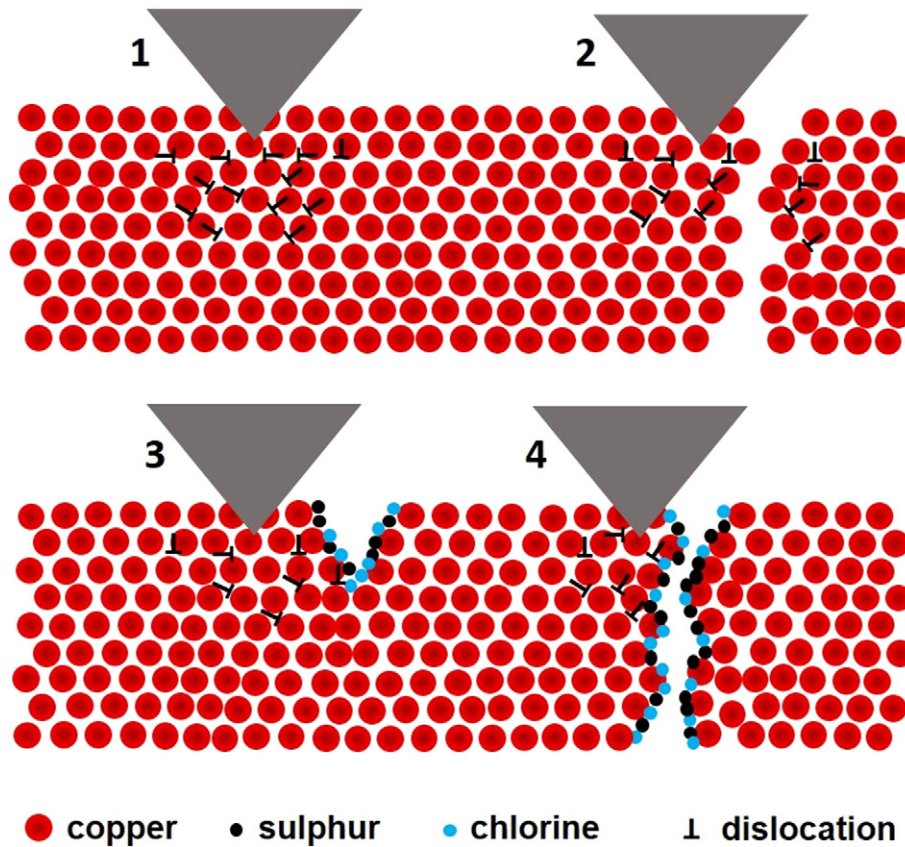


Fig. 9. The influence of the presence of a strong interface involving ionic bonding of copper with Cl and S species is illustrated. Dislocation motion is not hindered when indenting in the grain interior (1) and boundaries without the presence of inorganic species (2). In comparison, dislocation shielding is possible when it comes to a twin boundary (3) and HAGB (4) with segregated Cl and S atoms. Note: atoms not drawn to scale.

inorganic atomic species (Cl and S) on the global and local scales. At the local scale, surface topography was taken into account in order to report reliable hardness and elastic modulus values concerning the influence of boundaries. Nanoindentation experiments revealed that within the grain interior Films A and B showed a very similar plastic deformation behaviour, leading to about the same hardness value. A distinct difference was observed for indentation experiments performed at microstructural twin boundaries and HAGB. Film A, containing residual Cl and S in the ppm range showed a significantly higher hardness at twin boundaries and HAGB. Film B, an almost pure Cu film, showed no changes in hardness with respect to twin boundaries and HAGB. The difference can be attributed to the higher local impurity concentration at grain boundaries in Film A. Such interstitial atoms easily diffuse to the free surfaces and grain boundaries, forming strong bonds with the copper atoms. Interestingly, such high hardness was also observed at twin boundaries where the presence of impurities was indicated by the presence of distinct grooves. The almost pure Cu Film B exhibited no distinct differences between the grain interior and boundaries. Large errors in the obtained hardness can occur when the local topography matches the dimension (tip angle, contact depth) of the indenter tip or when microstructural features lead to imperfect indenter contact situations. These findings suggest that the RMS roughness value itself can be only treated as a global surface parameter where no general criteria can be established with respect to the validity of a performed nanoindentation. Instead, the presented experimental results show that the determination of accurate mechanical properties is strongly dependent on the local contact situation, which depends on the geometric relationship between the indenter shape (indenter geometry, final contact depth), the surface topography (curvature, grooves) and the local microstructure (grain boundaries). These influences can be well taken into account using the correlative procedure developed in this work.

Acknowledgement

The work was performed in the project EPPL, financially supported by grants from Austria, Germany, The Netherlands, France, Italy, Portugal, and the ENIAC Joint Undertaking (ENIAC JU Grant Agreement no. 325608). This project is co-funded within the programme “Forschung, Innovation und Technologie für Informationstechnologie” by the Austrian Ministry for Transport, Innovation and Technology.

References

- [1] S.P. Murarka, R.J. Gutmann, A.E. Kaloyerous, W.A. Lanford, Advanced multilayer metallization schemes with copper as interconnection metal, *Thin Solid Films* 236 (1993) 257–266.
- [2] R. Vinci, E. Zielinski, J. Bravman, Thermal strain and stress in copper thin films, *Thin Solid Films* 262 (1995) 142–153.
- [3] M. Nelhiebel, R. Illing, C. Schreiber, S. Wöhler, S. Lanzerstorfer, M. Ladurner, C. Kadow, S. Decker, D. Dibra, H. Unterwalcher, M. Rogalli, W. Robl, T. Herzig, M. Poschgan, M. Inselsbacher, M. Glavanovics, S. Fraissé, A reliable technology concept for active power cycling to extreme temperatures, *Microelectron. Reliab.* 51 (2011) 1927–1932.
- [4] M. Nelhiebel, R. Illing, T. Detzel, S. Wöhler, B. Auer, S. Lanzerstorfer, M. Rogalli, W. Robl, S. Decker, J. Fugger, M. Ladurner, Effective and reliable heat management for power devices exposed to cyclic short overload pulses, *Microelectron. Reliab.* 53 (2013) 1745–1749.
- [5] E.O. Hall, The deformation and ageing of mild steel: III discussion of results, *Proc. Phys. Soc. London, Sect. B* 64 (1951) 747.
- [6] N.J. Petch, The cleavage strength of polycrystals, *J. Iron Steel Inst.* 174 (1953) 25–28.
- [7] L. Lu, Y. Shen, X. Chen, L. Qian, K. Lu, Ultrahigh strength and high electrical conductivity in copper, *Science* 304 (2004) 422–426.
- [8] X.W. Zhou, H.N.G. Wadley, Twin formation during the atomic deposition of copper, *Acta Mater.* 47 (1999) 1063–1078.
- [9] C.K. Hu, B. Luther, F.B. Kaufman, J. Hummel, C. Uzoh, D.J. Pearson, Copper interconnection integration and reliability, *Thin Solid Films* 262 (1995) 84–92.
- [10] W.C. Oliver, G.M. Pharr, Measurement of hardness and elastic modulus by instrumented indentation: advances in understanding and refinements to methodology, *J. Mater. Res.* 19 (2004) 3–20.

- [11] J.L. Cuy, A.B. Mann, K.J. Livi, M.F. Teaford, T.P. Weihs, Nanoindentation mapping of the mechanical properties of human molar tooth enamel, *Arch. Oral Biol.* 47 (2002) 281–291.
- [12] P. Mondal, S.P. Shah, L. Marks, A reliable technique to determine the local mechanical properties at the nanoscale for cementitious materials, *Cem. Concr. Res.* 37 (2007) 1440–1444.
- [13] S. Hengsberger, A. Kulik, P. Zysset, Nanoindentation discriminates the elastic properties of individual human bone lamellae under dry and physiological conditions, *Bone* 30 (2002) 178–184.
- [14] S. Pathak, D. Stojakovic, S.R. Kalidindi, Measurement of the local mechanical properties in polycrystalline samples using spherical nanoindentation and orientation imaging microscopy, *Acta Mater.* 57 (2009) 3020–3028.
- [15] J. Ye, M. Kano, Y. Yasuda, Evaluation of local mechanical properties in depth in MoDTC/ZDDP and ZDDP tribochemical reacted films using nanoindentation, *Tribol. Lett.* 13 (2002) 41–47.
- [16] S.W. Wai, G.M. Spinks, H.R. Brown, M. Swain, Surface roughness: its implications and inference with regards to ultra microindentation measurements of polymer mechanical properties, *Polym. Test.* 23 (2004) 501–507.
- [17] M.S. Bobji, S.K. Biswas, Deconvolution of hardness from data obtained from nanoindentation of rough surfaces, *J. Mater. Res.* 14 (1999) 2259–2268.
- [18] Y. Xia, M. Bigerelle, S. Bovvier, A. Iost, P.-E. Mazeran, Quantitative approach to determine the mechanical properties by nanoindentation test: application on sandblasted materials, *Tribol. Int.* 82 (2015) 297–304.
- [19] J.-Y. Kim, S.-K. Kang, J.-J. Lee, J.-i. Jang, Y.-H. Lee, D. Kwon, Influence of surface-roughness on indentation size effect, *Acta Mater.* 55 (2007) 3555–3562.
- [20] M. Laurent-Brocq, E. Béjanin, Y. Champion, Influence of roughness and tilt on nanoindentation measurements: a quantitative model, *Scanning* 37 (2015) 350–360.
- [21] Y. Xia, M. Bigerelle, J. Marteau, P.-E. Mazeran, S. Bovvier, A. Iost, Effect of surface roughness in the determination of the mechanical properties of material using nanoindentation test, *Scanning* 36 (2014) 134–149.
- [22] J.-Y. Kim, J.-J. Lee, Y.-H. Lee, J.-i. Jang, D. Kwon, Surface roughness effect in instrumented indentation: a simple contact depth model and its verification, *J. Mater. Res.* 21 (2006) 2975–2978.
- [23] J. Jamari, D. Schipper, Deformation due to contact between a rough surface and a smooth ball, *Wear* 262 (2007) 138–145.
- [24] P. Berke, F. El Houdaigui, T. Massart, Coupled friction and roughness surface effects in shallow spherical nanoindentation, *Wear* 268 (2010) 223–232.
- [25] C. Walter, T. Antretter, R. Daniel, C. Mitterer, Finite element simulation of the effect of surface roughness on nanoindentation of thin films with spherical indenters, *Surf. Coat. Technol.* 202 (2007) 1103–1107.
- [26] M. Qasmi, P. Delobelle, Influence of the average roughness R_{ms} on the precision of the Young's modulus and hardness determination using nanoindentation technique with a Berkovich indenter, *Surf. Coat. Technol.* 201 (2006) 1191–1199.
- [27] W.-G. Jiang, J.-J. Su, X.-Q. Feng, Effect of surface roughness on nanoindentation test of thin films, *Eng. Fract. Mech.* 75 (2008) 4965–4972.
- [28] S. Bigl, S. Wurster, M.J. Cordill, D. Kiener, Advanced characterisation of thermo-mechanical fatigue mechanisms of different copper film systems for wafer metallisations, *Thin Solid Films* 612 (2016) 153–164.
- [29] W. Robl, M. Melzl, B. Weidgans, R. Hofmann, M. Stecher, Last metal copper metallization for power devices, *IEEE Trans. Semicond. Manuf.* 21 (2008) 358–362.
- [30] R. Saha, W.D. Nix, Effects of the substrate on the determination of thin film mechanical properties by nanoindentation, *Acta Mater.* 50 (2002) 23–38.
- [31] A. Wimmer, M. Smolka, W. Heinz, T. Detzel, W. Robl, C. Motz, V. Eyert, E. Wimmer, F. Jahnel, R. Treichler, G. Dehm, Temperature dependent transition of intragranular plastic to intergranular brittle failure in electrodeposited Cu micro-tensile samples, *Mater. Sci. Eng. A* 618 (2014) 398–405.
- [32] D.F. Bahr, D.E. Kramer, W.W. Gerberich, Non-linear deformation mechanisms during nanoindentation, *Acta Mater.* 46 (1998) 3605–3617.
- [33] W.C. Oliver, G.M. Pharr, An improved technique for determining hardness and elastic modulus using load and displacement sensing indentation experiments, *J. Mater. Res.* 7 (1992) 1564–1583.
- [34] K. Chavez, D. Hess, A novel method of etching copper oxide using acetic acid, *J. Electrochem. Soc.* 148 (2001) G640–G643.
- [35] D. Nečas, P. Klapetek, Gwyddion: an open-source software for SPM data analysis, *Cent. Eur. J. Phys.* 10 (2012) 181–188.
- [36] W.D. Nix, H. Gao, Indentation size effects in crystalline materials: a law for strain gradient plasticity, *J. Mech. Phys. Solids* 46 (1998) 411–425.
- [37] K. Durst, B. Backes, M. Göken, Indentation size effect in metallic materials: correcting for the size of the plastic zone, *Scr. Mater.* 52 (2005) 1093–1097.
- [38] J.J. Vlassak, W. Nix, Measuring the elastic properties of anisotropic materials by means of indentation experiments, *J. Mech. Phys. Solids* 42 (1994) 1223–1245.
- [39] H. Hertz, On the contact of rigid elastic bodies and on hardness, *Miscellaneous Papers*, Macmillan, London, 1886.
- [40] K.L. Johnson, *Contact Mechanics*, Cambridge University Press, 1987.
- [41] L.N. Sneddon, The relation between load and penetration in the axisymmetric Boussinesq problem for a punch of arbitrary profile, *Int. J. Eng. Sci.* 3 (1965) 47–57.
- [42] P.A. Korzhavyi, I.A. Abrikosov, B. Johansson, Theoretical investigation of sulfur solubility in pure copper and dilute copper-based alloys, *Acta Mater.* 47 (1999) 1417–1424.
- [43] D. Hull, D.J. Bacon, *Introduction to Dislocations*, Pergamon Press, Oxford, 1984.
- [44] W.W. Mullins, The effect of thermal grooving on grain boundary motion, *Acta Metall.* 6 (1958) 414–427.
- [45] J.W. Martin, R.D. Doherty, B. Cantor, *Stability of Microstructure in Metallic Systems*, Cambridge University Press, 1997.
- [46] A. Mersmann, *Crystallization Technology Handbook*, CRC Press, 2001.
- [47] A.E.N.N. Greenwood, *Chemistry of Elements*, Pergamon Press, Oxford, 1984.